Volume 6
Number 5
7 February 2018
Pages 911-1266

Journal of
Materials Chemistry C

Materials for optical, magnetic and electronic devices

rsc.li/materials-c

ISSN 2050-7526

PAPER
Nosang V. Myung, Yong-Ho Choe et al.
A noble gas sensor platform: linear dense assemblies of single-walled carbon nanotubes (LA-CNTs) in a multi-layered ceramic/metal electrode system (MLES)

ROYAL SOCIETY
OF CHEMISTRY

rsc.li/materials-c

1 Molecular Engineering, Synthesis, and Atomistic Structure-Property
2 Relationship of Indoloquinoxaline-Capped Small Donors for Efficient
3 Organic Solar Cells

4 Maryam Javed[1], Waqas Akram[1,2], Zeeshan Ali[1], Nabeel Shahzad[3], Munazza Shahid[4*],

5 Ghayoor Abbas Chotana[5], Jafar Iqbal Khan[6], Jie Min[7], Muhammad Altaf[1], Christian B.

6 Nielsen[8*], Raja Shahid Ashraf[1*]

7 [1]Department of Chemistry, Institute of Chemical Sciences, Government College University

8 Lahore, Punjab 54000, Pakistan

9 [2]Department of Chemistry, University of Agriculture, Faisalabad, 38000, Pakistan

10 [3]Department of Chemistry, Government College University, Faisalabad 38000, Pakistan

11 [4]Department of Chemistry, University of Education, Bank Road Campus, Lahore, Punjab

12 54000, Pakistan

13 [5]Department of Chemistry and Chemical Engineering, Lahore University of Management

14 Sciences, Lahore, Punjab 54792, Pakistan

15 [6]Department of Physics, School of Natural Sciences, University of Hull, Hull HU6 7RX, UK

16 [7]The Institute for Advanced Studies, Wuhan University, Wuhan 430072, China

17 [8]Department of Chemistry, School of Physical and Chemical Sciences, Queen Mary

18 University of London, London E1 4NS, UK

19 Corresponding author(s); munazza.shahid@ue.edu.pk; c.b.nielsen@qmul.ac.uk;

20 rajashahid@gcu.edu.pk;

21 Abstract

22 The growing demand for high-performance organic photovoltaics has sparked great interest in
23 small-molecule donor (SMD) materials that offer well-defined structures and superior batch-
24 to-batch consistency. In this study, we report the molecular design, synthesis, and atomistic
25 structure-property characterization of three indoloquinoxaline (IQ)-capped SMDs named as
26 DPP-Th-IQ, BT-Th-IQ, and TT-IQ for potential applications in all-small-molecule organic
27 solar cells (ASM-OSCs). Each SMD features a distinct central core, including
28 diketopyrrolopyrrole (DPP), benzothiadiazole (BT), or thieno[3,2-b]thiophene (TT) with
29 thiophene as bridging units in the DPP and BT derivatives, to systematically tune electronic
30 structures, optical profiles, and charge transport properties. Electrochemical analysis confirmed
31 that all three SMDs possess well-aligned HOMO-LUMO levels conducive to pairing with the
32 Y6 non-fullerene acceptor. Density functional theory (DFT) calculations revealed low
33 hole/electron reorganization energies with extensive frontier-orbital delocalization, indicative
34 of efficient charge transport. Photophysical experiments based on UV-Vis, photoluminescence,
35 and solvatochromic analysis and complementary computational characterization showed
36 strong intramolecular charge transfer in SMDs. Electron density difference analysis explained
37 that particularly benzothiadiazole-based BT-Th-IQ donor exhibits the lowest exciton binding
38 energy coupled with high charge transfer excitations, indicating efficient exciton dissociation.
39 Donor-acceptor interfacial modeling further predicted robust face-on π–π stacking and
40 favorable donor-Y6 orientations that support interfacial charge transfer. Importantly, all three
41 SMDs demonstrated initial thin-film stability: films retained ≥ 90% of their initial absorbance
42 after 30 hours of continuous AM 1.5G irradiation, and thermogravimetric analysis showed
43 decomposition temperatures (5% weight loss) exceeding 250 °C. Overall, this study clarifies

44 the interplay between molecular design, electronic structure, interfacial interactions, and
45 stability, providing a strategic path toward next-generation high-efficiency ASM-OSCs based
46 on IQ-capped donors.

47 **Keywords:** Organic Solar Cells; Small-Molecule Donors; Indoloquinoxaline; Synthesize;
48 Density Functional Theory

1. Introduction

50 The continuously growing global demand for sustainable energy has accelerated research and
51 development in advanced photovoltaic technologies. Among the various platforms, organic
52 solar cells (OSCs) have garnered particular attention due to their potential for lightweight,
53 flexible, and cost-effective energy harvesting devices. In contrast to certain hybrid perovskite
54 and dye-sensitized solar cells that may employ toxic or corrosive materials, OSCs present a
55 more environmentally benign alternative, relying on carbon-based materials with relatively
56 lower toxicity profiles.[1-3] Early OSCs primarily utilized fullerene acceptors paired with small
57 molecular donors, attaining modest yet promising power conversion efficiencies (PCEs).
58 However, limitations such as narrow absorption coefficients, constrained energy-level
59 tunability, and suboptimal thermal stabilities restricted these devices to PCE values of about
60 13%.[4]

61 Subsequent developments focused on the integration of non-fullerene acceptors (NFAs), which
62 helped push OSC efficiencies above 20%.[5-6] NFAs offer advantages such as wider absorption
63 ranges, customizable bandgaps, and improved morphological stability. Yet, pairing NFAs with
64 polymer-based donors introduces additional complexities, with most notably polydispersity
65 and potential morphological instabilities that may limit device reproducibility and long-term
66 performance. In response, small molecular donors (SMDs) have emerged as compelling
67 alternatives, owing to their well-defined molecular structures, tunable electronic structures for
68 optimal donor-acceptor alignment, and batch-to-batch consistency. Nonetheless, despite these
69 attributes, all-small-molecule OSCs (ASM-OSCs) continue to trail polymer–NFA systems in
70 terms of overall efficiency, with most reports hovering around 15–16% PCE.[7-9] This
71 discrepancy underscores the need for new small molecular donor designs that not only rival
72 polymer-based donors but also surpass existing challenges related to morphology, stability, and
73 scalability.

74 Molecular design strategies for small-molecule donors often involve A–D–A or A–π–D–π–A
75 backbones, where electron-rich (donor) and electron-deficient (acceptor) units are carefully
76 arranged to optimize energy-level alignment and facilitate efficient charge transfer. Building
77 blocks like benzo-[1,2-b:4,5-b′]dithiophene (BDT) have been widely adopted due to their
78 planar geometry, which enhances molecular packing and charge mobility.[10] Early BDT-
79 containing donors achieved moderate PCEs when combined with fullerene acceptors, while
80 subsequent efforts pairing BDT-based donors with high-performance Y6-type NFAs have
81 driven ASM-OSC efficiencies beyond 15%.[11-13] Other core motifs, such as naphtho[1,2-b:5,6-
82 b′]dithiophene, porphyrins, and thienobenzo-dithiophene (TBD), extend the available chemical
83 space, enabling systematic fine-tuning of optical properties and energy levels.[14-16] Although
84 these structural innovations have improved ASM-OSC performance, several practical issues
85 persist. For example, many small-molecule donors lack the favorable film-forming
86 characteristics inherent to polymers, necessitating additional processing or post-treatment steps
87 to achieve optimal domain sizes and morphologies in the active layer. Moreover, certain small-
88 molecule donors are prone to crystallization or self-aggregation, which, if not properly
89 controlled, can hinder charge transport and limit device reproducibility.

90   Despite the advancements, the morphology of ASM-OSCs remains difficult to control.
91   Achieving a continuous, yet finely mixed donor–acceptor network typically demands post-
92   treatments (e.g., thermal or solvent vapor annealing) that may be unsuitable for large-scale
93   manufacturing.[16] Moreover, the low viscosity of small-molecule solutions complicates large-
94   area printing of photoactive layers, posing a hurdle for industrial fabrication. Finally, although
95   polymer-based materials often show greater morphological stability, questions persist
96   regarding the long-term reliability of fully small-molecule systems.[17] Systematic stability
97   studies will be integral as the field advances. Therefore, ASM-OSCs remain in a stage of
98   ongoing materials exploration and efficiency enhancement, and more comprehensive answers
99   to existing challenges may only emerge as a wider variety of donor–acceptor combinations are
100   investigated. Progress is particularly dependent on the careful molecular engineering of small-
101   molecule donors and acceptors to optimize key photovoltaic parameters: open-circuit voltage
102   (V_{OC}), short-circuit current density (J_{SC}), and fill factor (FF). Achieving V_{OC} values above 0.90
103   V requires precise control of the donor's highest occupied molecular orbital (HOMO) and the
104   acceptor's lowest unoccupied molecular orbital (LUMO) energy levels, while broad absorption
105   spectra and high charge-carrier mobility are essential to maximizing both J_{SC} and FF.[18-20]
106   Consequently, the primary obstacle lies in designing donor-acceptor (D/A) systems with
107   aligned energy levels, extended absorption across the visible to near-infrared region, and robust
108   morphological and electronic properties. Addressing this challenge necessitates the discovery
109   and development of efficient SMDs that not only meet these stringent performance criteria but
110   also enhance device stability, thereby paving the way for future efficient ASM-OSCs.

111   This study reports the design, synthesis, and computational characterization of three new SMDs
112   based on indoloquinoxaline (IQ) end-groups and two electron-deficient central cores, including
113   diketopyrrolopyrrole (DPP), and benzothiadiazole (BT), one electron-rich core,
114   thienothiophene (TT) and named as DPP-Th-IQ, BT-Th-IQ, and TT-IQ, respectively. IQ-based
115   architecture has recently garnered increasing interest. The intrinsic donor–acceptor character
116   of 6H-indolo[2,3-b] quinoxaline, which is derived from electron-rich indole ring and electron-
117   deficient quinoxaline fragment facilitates efficient intramolecular charge transfer (ICT),
118   making it a promising terminal unit in SMD design. Among central units, DPP stands out for
119   its robust electron-transporting capacity, high photochemical stability, and strong absorption,
120   whereas BT is a versatile acceptor fragment easily synthesized from readily available
121   precursors. Both DPP- and BT-centered molecules are further modified with thiophene π-
122   bridges to extend conjugation and fine-tune energy levels. By contrast, TT central unit imparts
123   a rigid backbone that is conducive to planar packing and efficient π-π interactions, potentially
124   boosting charge mobility and light absorption. By systematically examining the structural,
125   optical, electrochemical, and charge transfer (CT) properties of these IQ-capped donors with
126   distinct core units, we aim to clarify structure-property relationships at atomistic level and
127   highlight promising design principles for next-generation ASM-OSCs.

128   2. Materials and Methods

129   Materials and Instruments

130   All reagents and catalysts were purchased from Sigma-Aldrich and Tokyo Chemical Industry
131   and used without further purification. Solvents, including dichloromethane (DCM), ethyl
132   acetate, and n-hexane, were procured from local vendors and distilled prior to use. Melting
133   points were determined using a Jindal melting point apparatus with open capillary tubes. ^{1}H
134   and ^{13}C NMR spectra were recorded on a Bruker Ascend 400 MHz spectrometer, employing
135   deuterated chloroform (CDCl$_3$) as the solvent and trimethylsilane (TMS) as an internal
136   reference. The IR spectra were recorded using a Bruker Alpha Platinum ATR spectrometer.

137 The UV-Vis absorption spectra were obtained using a Shimadzu Pharmaspec UV-1700
138 spectrophotometer in both solutions and solid films and photoluminescence (PL) spectra were
139 measured using a Cary Eclipse Fluorescence Spectrophotometer. Photostability tests were
140 performed under continuous AM 1.5G illumination (100 mW cm⁻²) using a G2V Optics Pico™
141 LED solar stimulator. Perkin Elmer USA, model STA 8000 device was used to examine the
142 stability of compounds at varied temperatures (20-120 °C). In a nitrogen atmosphere, at a
143 heating rate of 10 °C/min thermogravimetric analysis (TGA) was performed in the temperature
144 range of 30 °C to 700 °C. For cyclic voltammetry measurements, a standard three-electrode
145 configuration was employed in a PalmSens EmStat3+ potentiostat, using Ag/AgCl as the
146 reference electrode, Fluorine-doped Tin Oxide (FTO) glass as the working electrode, and
147 ferrocene as an internal reference.

Computational Methodology

149 Density Functional Theory (DFT) and Time-Dependent DFT (TD-DFT) calculations were
150 carried out with Gaussian 09 software.[21-24] B3LYP hybrid functional combined with the 6-
151 31G(d,p) basis set was employed to model molecular geometries and electronic structures.[25-26]
152 Vibrational frequency calculations were performed to confirm that all geometries correspond
153 to local minima on the potential energy surface. For electronic structures, Mulliken population
154 analysis was employed to investigate the contributions of individual molecular fragments to
155 the frontier molecular orbitals (FMOs). Furthermore, the density of states (DOS) and partial
156 density of states (PDOS) of the molecular units in the donors were analyzed using PyMOlyze-
157 1.1 software.[27] The solvent-phase absorption spectra was simulated by CAM-B3LYP/6-31G
158 (d,p) method with IEFPCM model and Gibbs solvation free energy (ΔG_{solv}) was simulated
159 using the SMD model by M06-2X/6-31G (d,p) method.[28]

160 Electron density difference (EDD) analysis were conducted for every optimized SMD and
161 SMD/acceptor complexes in order to visualize the redistribution of charge upon
162 photo-excitation and to extract quantitative charge transfer descriptors.[21, 29] Following
163 Le Bahers *et al.* and the Multiwfn 3.8 implementation, four primary quantities given in
164 **Equation 1-4** were evaluated from the difference density $\Delta\rho(r)=\rho_{ele}(r)-\rho_{hole}(r)$:[21, 30]

$$D_{CT} = |R_{ele} - R_{hole}| \, ; R_{ele/hole} = \frac{\int \rho_{ele/hole}(r)rdr}{\int \rho_{ele/hole}(r)dr} \quad (1)$$

$$q_{CT} = \frac{1}{2}\int |\rho_{ele}(r) - \rho_{hole}(r)|dr \quad (2)$$

$$D_{index} = \frac{\sum_i \rho_{ele}i \, \rho_{hole}i \, |r_i - R_{hole}|}{\sum_i \rho_{ele}i \, \rho_{hole}i} \quad (3)$$

$$t_{index} = D_{CT} - H_{index} \quad (4)$$

169 where D_{CT} is the electron-hole centroid separation among the barycentre, q_{CT} the total
170 transferred charge magnitude. Whereas, the indices H_{index}/t_{index} were used to evaluate charge
171 transition behavior and the extent of charge separation. H_{index} is the spatial extent of the
172 transition along the CT axis, and t_{index} is a separation metric that approaches zero when electron
173 and hole strongly overlap. Through-space CT mechanism was examined based on these EDD
174 parameters. In practice, higher D_{CT} together with large q_{CT} and low H_{index} is taken as an
175 indicator of efficient spatial charge separation.

176 For each excited state the Inter-Fragment Charge-Transfer (IFCT) matrix was built and the
177 relative contributions of charge-transfer and local excitations were obtained from **Equation 5**
178 and **6**:

179
$$CT(\%) = \frac{\sum_{D \neq A} q_{D \to A}}{\sum_{all} q_{i \to j}} \times 100 \quad (5)$$

180
$$LE(\%) = 100 - CT(\%) \quad (6)$$

181 where $q_{D \to A}$ is the electron population transferred from donor fragment D to acceptor fragment
182 A.

183 A large D_{CT} or CT(%) combined with a small H_{index}, t_{index} and LE(%) evidences efficient charge
184 separation and, by extension, a reduced probability of geminate and non-geminate
185 recombination in organic photovoltaic materials. In addition, the transition density matrix
186 (TDM) and hole/electron overlap heat maps were generated to visualize electron–hole
187 coherence across molecular fragments in SMDs.[30-31] All EDD and IFCT quantities were
188 obtained directly via Multiwfn 3.8 on excited-state wave-functions calculated using the range-
189 separated hybrid (RSH) functional "CAM-B3LYP".[32-35]

190 The charge transport capabilities of the materials were assessed by calculating reorganization
191 energy, a key parameter for estimating charge carrier mobility in organic materials. The
192 adiabatic potential energy surface (PES) approach was used to compute the reorganizational
193 energy of holes (λ_{hole}) and electrons (λ_{ele}), respectively.[36-37] These values were derived based
194 on the relaxation of the cationic and anionic states to the neutral molecular geometry, as defined
195 by the following **Equation 7** and **8**:

196
$$\lambda_{hole} = (E^+_{neutral} - E_{neutral}) + (E_{cationic} - E^0_{cationic}) \quad (7)$$
197
$$\lambda_{ele} = (E^-_{neutral} - E_{neutral}) + (E_{anionic} - E^0_{anionic}) \quad (8)$$

198 Where, $E_{neutral}$ represents the neutral molecule energy, $E^+_{neutral}$ and $E^-_{neutral}$ are the cationic
199 and anionic states energies optimized from the neutral geometry, while $E_{cationic}$ and $E_{cationic}$
200 denote the cationic and anionic states energies, respectively. Whereas, $E^0_{cationic}$ and $E^0_{anionic}$
201 correspond to the energy of the neutral molecule optimized in the cationic and anionic
202 geometries, respectively.

3. Results and Discussion

Synthesis

205 The synthesis of side-peripheral **IQ** groups was carried out with the preparation of 8-bromo-
206 6H-indolo[2,3-b] quinoxaline derivatives via a straightforward condensation reaction, as
207 previously described in the literature.[38] This involved the reaction of 1,2-diaminobenzene with
208 6-bromoindoline-2,3-dione in glacial acetic acid under reflux, yielding the target compound in
209 a high yield of 87%. To improve the solubility and processability of the rigid-structured fused-
210 ring IQ derivatives, N-alkylation was performed using 2-ethylhexyl bromide and potassium
211 carbonate in dimethylformamide at 80°C overnight, resulting in the formation of 8-bromo-6-
212 (2-ethylhexyl)-6H-indolo[2,3-b]quinoxaline (**C₈IQa**). Subsequent borylation was carried out
213 using bis(pinacolato)diboron as the borylating agent, in the presence of palladium acetate, X-
214 Phos as the catalyst, and potassium acetate as the base, resulting in 6-(2-ethylhexyl)-8-(4,4,5,5-
215 tetramethyl-1,3,2-dioxaborolan-2-yl)-6H-indolo[2,3-b]quinoxaline (**C₈IQb**), as given in
216 **Scheme 1**.

217 Small molecular donors with DPP, BT, and TT cores were synthesized with IQ moieties as
218 terminal groups through different synthesis pathways. Thiophene was used as a bridging unit
219 in the DPP- and BT-based donor derivatives, while the TT-based derivative synthesised
220 without the bridging thiophene units, as illustrated in **Scheme 1**. The donor molecule 2,5-bis(2-

221 ethylhexyl)-3,6-bis(5-(6-(2-ethylhexyl)-6H-indolo[2,3-b]quinoxalin-8-yl)thiophen-2-yl)-2,5-
222 dihydropyrrolo[3,4-c]pyrrole-1,4-dione (DPP-Th-IQ) was synthesized starting from 3,6-
223 di(thiophen-2-yl)-2,5-dihydropyrrolo[3,4-c]pyrrole-1,4-dione. Initially, N-alkylation of the
224 DPP core was achieved by reacting 2-ethylhexyl bromide with potassium carbonate in DMF at
225 80°C for 24 hours, producing 2,5-bis(2-ethylhexyl)-3,6-di(thiophen-2-yl)-2,5-
226 dihydropyrrolo[3,4-c]pyrrole-1,4-dione. Bromination of this intermediate with N-
227 bromosuccinimide (NBS) in DMF at 60°C overnight yielded (**1**). Finally, the target DPP-Th-
228 IQ donor was synthesized through Suzuki-Miyaura cross-coupling reaction between **1** and
229 **C$_8$IQb** in the presence of a palladium catalyst, resulting in a 57% yield after purification. The
230 BT-based donor, 4,7-bis(5-(6-(2-ethylhexyl)-6H-indolo[2,3-b]quinoxalin-8-yl)thiophen-2-
231 yl)benzo[c][1,2,5]thiadiazole (BT-Th-IQ), was synthesized starting from 4,7-
232 dibromobenzo[c][1,2,5]thiadiazole (DBBT). Initially, a Stille coupling reaction was performed
233 between DBBT and tributyl(thiophen-2-yl)stannane in the presence of
234 dichlorobis(triphenylphosphine)palladium(II) as the catalyst and tetrahydrofuran (THF) as the
235 solvent, yielding (**2**). Direct arylation (C–H activation) of **2** with **C$_8$IQa** yielded the final BT-
236 Th-IQ donor in a 78% yield. Whereas, the TT-based donor, 2,5-bis(6-(2-ethylhexyl)-6H-
237 indolo[2,3-b]quinoxalin-8-yl)thieno[3,2-b]thiophene (TT-IQ), was synthesized in a single step
238 via Stille coupling. This involved the reaction of 2,5-bis(tributylstannyl)thieno[3,2-b]thiophene
239 (**3**) with the prepared brominated IQ derivative **C$_8$IQa** using
240 dichlorobis(triphenylphosphine)palladium(II) as the catalyst in THF. The reaction afforded
241 TT-IQ in high yield (87%) after purification. The chemical structures of synthesized
242 intermediates and compounds were confirmed by ^{1}H NMR and ^{13}C NMR spectroscopy, and
243 the corresponding spectra are provided in the Supporting Information (**Figure S1-S9**), along
244 with detailed reaction kinetics.

245
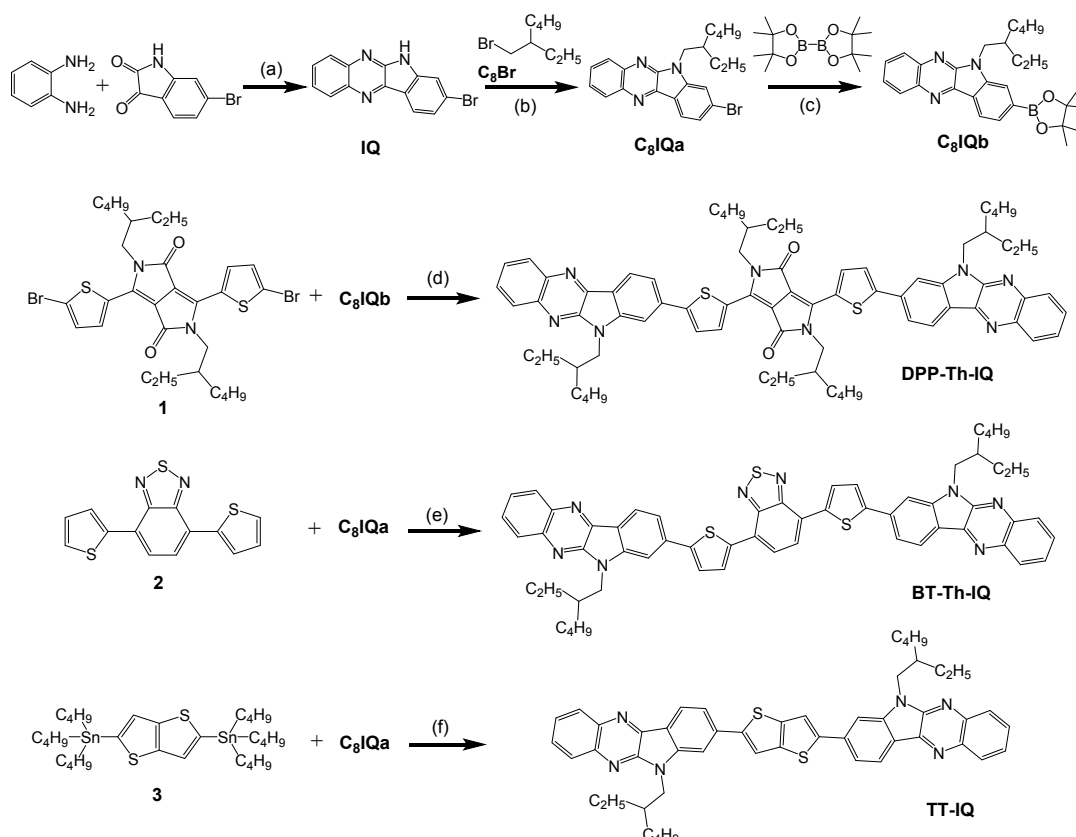
246 **Scheme 1.** Synthesis pathway of diketopyrrolopyrrole (DPP), benzothiadiazole (BT), and thieno[3,2-
247 b]thiophene (TT) core units containing small molecular donors: (a) glacial acetic acid, DMF, reflux
248 24 h, (yield, 87%) (b) 2-ethylhexyl bromide, K$_2$CO$_3$, DMF, 85 °C, 18 h, (yield, 80%) (c)

249   bis(pinacolato)diboron, Pd(CH$_3$COO)$_2$, X-Phos, CH$_3$CO$_2$K, toluene, 85 °C, 14 h (yield, 75%) (d)
250   Pd(CH$_3$COO)$_2$, X-Phos, K$_2$CO$_3$, THF/water, 85 °C, 18 h (yield, 57%) (e)Pd(CH$_3$COO)$_2$, K$_2$CO$_3$,
251   Pivalic acid, PCy$_3$.HBF$_4$ ligand, DMA, 110 °C, 5h (yield, 78%) (f) PdCl$_2$(PPh$_3$)$_2$, THF, 65 °C, 24 h
252   (yield, 87%).

Energy Levels and Estimated Driving-Force Offsets

254   An understanding of the HOMO and LUMO energies is paramount when designing efficient
255   D/A systems for BHJ-OSCs. In particular, the donor's HOMO must be sufficiently deep to
256   maximize the V$_{OC}$ of OSCs, while the donor's LUMO should be higher than that of the acceptor
257   to facilitate efficient electron transfer and prevent back-electron transfer.[39-40] **Table 1** provides
258   the electrochemical properties of the newly synthesized IQ-capped SMDs based on the CV
259   experiments alongside the benchmark Y6 NFA. For insights into the redox behavior and energy
260   levels estimation of the synthesized SMDs, CV measurements were carried out in anhydrous
261   dichloromethane (5 mL) containing 2 mM of the analyte and 0.1 M tetrabutylammonium
262   hexafluorophosphate (TBAPF$_6$) as the supporting electrolyte, at a scan rate of 50 mVs^{-1}. The
263   solutions were purged with dry N$_2$ for 5 min prior to measurements. Oxidation (E_{ox}^{onset}) and
264   reduction (E_{red}^{onset}) onsets were referenced to the ferrocene/ferrocenium redox couple (Fc/Fc$^+$),
265   assuming an absolute HOMO of 4.88 eV for Fc/Fc$^+$. CV profiles and an energy-level diagrams
266   comparing SMDs to Y6 are shown in **Figure 1a-1d**. Whereas, the CV profiles of the SMDs
267   with the labelled oxidation and reduction potential values are given in the Supporting
268   Information **Figure S10 a-c**.

269   From the CV results, we inferred that DPP-Th-IQ exhibited an oxidation onset (E$_{ox}$) of
270   approximately 1.05 V and a reduction onset (E$_{red}$) of -0.67 V, leading to a calculated HOMO
271   energy (E$_H$) of -5.35 eV and LUMO energy (E$_L$) of -3.70 eV. The electrochemical bandgap (
272   E_g^{CV}) was thus 1.65 eV, which is almost consistent with optical bandgap (E_g^{opt}) of 1.71 eV, TT-
273   IQ showed a slightly lower oxidation potential but a more negative reduction potential of -0.87
274   V, indicative of the electron-rich thieno[3,2-b]thiophene core's influence on the redox
275   behavior. The E$_H$ and E$_L$ were determined to be -5.30 eV and -3.44 eV, respectively, and the
276   E_g^{CV} was observed as 1.86 eV. Whereas BT-Th-IQ, incorporating the electron rich BT fragment,
277   exhibited the lowest oxidation onset at 0.91 V and a reduction onset of -0.95 V, resulting in E$_H$
278   of -5.13 eV and E$_L$ of -3.35 eV. While the E_g^{CV} of BT-Th-IQ SMD was estimated as 1.78 eV,
279   almost consistent with the E_g^{opt} 1.85 eV based on the onset absorption spectra (**Table 1**). Small
280   disparity in bandgaps reflect intra- and intermolecular interactions that shift the absorption edge
281   in thin films. Overall, the deeper E$_H$ (around -5.3 to -5.4 eV) of DPP-Th-IQ and TT-IQ suggest
282   a higher attainable V$_{OC}$ compared to BT-Th-IQ, yielding a shallower E$_H$ (-5.13 eV) which could
283   reduce the maximum achievable voltage in cell device. Meanwhile, all three SMDs have E$_L$
284   well above that of Y6 (-4.1 eV),[41] ensuring a sufficient offset for exciton dissociation at D/A
285   interface as shown in **Figure 1c-1d**.

286   The V$_{OC}$ was estimated by pairing the SMDs with benchmark Y6 acceptor based on the
287   Scharber relation, which incorporates the donor's E$_H$ and the acceptor's E$_L$ along with an
288   empirical offset of 0.3 V for charge separation. Under these assumptions, DPP-Th-IQ and TT-
289   IQ both resulted in relatively high predicted V$_{OC}$ values of 0.95 and 0.90 V, respectively. By
290   contrast, BT-Th-IQ exhibited a lower estimated V$_{OC}$ of 0.73 V, owing to its upshifted HOMO
291   and comparatively smaller HOMO-LUMO offset with Y6. Efficient exciton dissociation in
292   OSCs typically requires a minimum energy offset of ~0.2–0.3 eV between the donor and
293   acceptor LUMOs (ΔE_{L-L}) and often an analogous offset in HOMOs (ΔE_{H-H}).[42] Here, all three
294   SMDs demonstrated sufficient LUMO energy offsets with Y6 NFA, such as DPP-Th-IQ, BT-
295   Th-IQ, and TT-IQ showcased the offsets of 0.40 eV, 0.75 eV, and 0.66 eV, respectively.

296   Although a larger offset favors electron transfer, it can also lead to energy losses that lower the
297   V_{OC} as demonstrated in interfacial CT mechanism in **Figure 1b**. This trade-off is exemplified
298   by BT-Th-IQ, which has the largest ΔE_{L-L} of 0.75 eV but the lowest predicted V_{OC} value of
299   0.73 V. In contrast, DPP-Th-IQ exhibited a balanced approach maintaining a sufficient LUMO
300   offset of 0.40 eV for electron transfer while preserving a relatively high potential for V_{OC}. From
301   device engineering perspective, the ideal D/A pair balances a minimal energy offset to reduce
302   voltage losses with sufficient offset to drive exciton dissociation and minimize charge
303   recombination. Thus, while BT-Th-IQ can provide robust electron-driving potential, its
304   upshifted HOMO level poses a challenge for maximizing V_{OC}. Conversely, DPP-Th-IQ and
305   TT-IQ exhibited deeper HOMOs with adequate LUMO offsets, indicating promise for higher
306   V_{OC} alongside efficient charge generation.

307 **Table 1.** Electronic structure parameters and energy-driving potential of designed DPP-, BT-, and TT-
308 based donor molecules when blended against the benchmark Y6 acceptor. The V_{OC} and driving-force
309 offsets for Y6 acceptor were evaluated against polymer donor PM6.[41]

Molecule	E_H (eV)[a]	E_L (eV)[a]	E_g^{CV} (eV)[b]	E_g^{opt} (eV)[d]	V_{OC} (V)[e]	ΔE_{L-L} (eV)[f]	ΔE_{H-H} (eV)[f]
DPP-Th-IQ	-5.35	-3.70	1.65	1.71	0.95	0.4	0.35
BT-Th-IQ	-5.13	-3.35	1.78	1.85	0.73	0.75	0.57
TT-IQ	-5.30	-3.44	1.86	1.96	0.9	0.66	0.4
Y6	-5.65	-4.10	1.60	1.51	1.1	0.54	0.2

310   [a]HOMO and LUMO energy level (E_H and E_L, respectively) as determined by the oxidation (E_{ox}^{onset})
311   and reduction onsets (E_{red}^{onset}) by CV via relation $E_{HOMO} = -\left(E_{ox}^{onset} - E_{Fc}^{onset} + 4.8\right) eV$ and E_{LUMO}
312    $= -\left(E_{red}^{onset} - E_{Fc}^{onset} + 4.8\right) eV$; [b]Energy bandgap ($E_g^{CV}$) determined from the CV calculations via
313   relation $E_g^{CV} = E_H - E_L$; [c]Energy bandgap (E_g^{opt}) determined by the onset spectra in the solution;
314   [d]Energy bandgap (E_g^{opt}) determined by the onset spectra in thin film ; [e]Open-circuit voltage (V_{OC})
315   evaluated via Scharber relation as $V_{OC} = \frac{E_{H(donor)} - E_{L(acceptor)}}{e} - 0.3$, where E_L is LUMO of acceptor, E_H
316   is HOMO level of donor, e is the elementary charge, and 0.3 V is an empirical factor for charge
317   separation; [f]ΔE_{L-L} is the energy difference between E_L of acceptor to E_L of the donor, while ΔE_{H-H} is
318   the energy difference from E_H of acceptor to E_H of the donor.
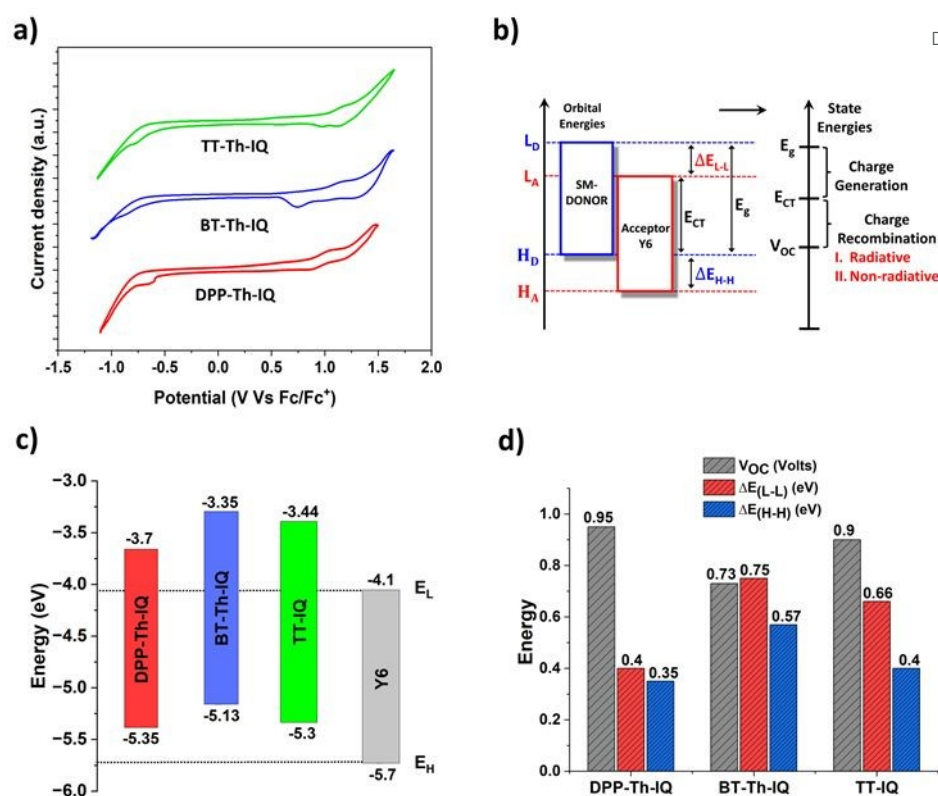
Journal of Materials Chemistry C

Figure 1. Cyclic voltammograms of SMDs measured in anhydrous dichloromethane (5 mL) containing 2 mM of the analyte and 0.1 M tetrabutylammonium hexafluorophosphate (TBAPF$_6$) as the supporting electrolyte, at a scan rate of 50 mVs^{-1}. (b) Energy levels diagram representing HOMO/LUMO energy levels of donor (H$_D$/L$_D$) and HOMO/LUMO energy levels acceptor (H$_A$/L$_A$) for feasible charge transfer mechanism in photoactive configuration. (c) Energy levels diagram and (d) estimated open-circuit voltage (V$_{OC}$) based on Scharber relation with respective driving-force offsets of the SMDs against benchmark Y6 NFA.

Electronic Structure Properties

To elucidate how molecular geometry and electronic configuration influence the performance of the synthesized IQ-capped SMDs, DFT calculations were performed at B3LYP/6-31G(d,p) level of theory. **Figure 2a** presents the optimized geometry, highlighting the dihedral angles between the IQ end-groups, any bridging thiophene rings, and the central cores. In DPP-Th-IQ, the IQ–thiophene and thiophene-DPP core dihedral angles are 25.2° and 11.1°, respectively. In BT-Th-IQ, the IQ-thiophene dihedral measures 25.7°, whereas the thiophene–BT core dihedral is 8.5°. Larger angels between side IQs and thiophene bridges are due to steric repulsions among neighboring hydrogen atoms of fused benzene IQ units and thiophenes. The TT-IQ, which lacks bridging thiophene rings, exhibited IQ-TT core dihedral of 26.1°. Overall, the SMDs exhibited quasi-coplanar arrangements which can partially reduce π-conjugation but geometry is sufficient for effective ICT and electronic delocalization.

Molecular electrostatic potential (MESP) maps given in **Figure 2b** further revealed distinct regions of positive (blue) and negative (red) potential, corresponding to electron-deficient and electron-rich moieties, respectively.[43] Across the three SMDs, the electronegative atoms (nitrogen in IQ and sulfur in the core/thiophene) tend to attract electron density to produce negative potential localized pockets. Simultaneously, the alkyl-substituted fragments and less electronegative regions appeared as positive potential zones. This spatial variation in electrostatic potential not only corroborates the partial donor–acceptor character inherent to

346 each molecule but also rationalize the observed CT pathways. Regions exhibiting strongly
347 negative potential often overlap with segments that accept electron density in the LUMO,
348 whereas areas of positive potential align with electron-rich sites in the HOMO and provide a
349 complementary perspective on how holes/electrons may be distributed/transferred upon
350 excitation.

351 Furthermore, the FMOs analysis based on delocalization of HOMOs and LUMOs given in
352 **Figure 2c** and PDOS graphs based on Mulliken analysis in **Figure 2d** showed that the HOMOs
353 of DPP-Th-IQ and TT-IQ delocalize on electron-rich cores (≈58% for DPP-Th-IQ and ≈52%
354 for TT-IQ). Whereas, the BT-Th-IQ's HOMO is more evenly distributed between the core
355 (≈25%) and thiophenes (≈49%). Such a broad HOMO delocalization can improve hole
356 mobility, an essential feature for efficient donors in OSCs.[44-45] In contrast, the LUMOs of the
357 SMDs exhibited varied localization. BT-Th-IQ's LUMO (≈68%) on the core reflects the strong
358 electron-withdrawing character of benzothiadiazole, while TT-IQ's LUMO lies predominantly
359 on the IQ end-groups (≈80%). DPP-Th-IQ displayed a more balanced LUMO distribution
360 across the central DPP core, bridging thiophenes, and IQ terminal. These results are
361 summarized in Supporting Information **Table S1**. Although torsional angles introduce partial
362 breaks in π-conjugation, the inherent donor–acceptor motif promotes a robust ICT pathway, as
363 evidenced by the even frontier-orbital delocalization and PDOS patterns. Moreover, comparing
364 the DFT-derived HOMO–LUMO gaps with experimentally measured electrochemical
365 bandgaps (**Table 1**) shows consistent trends and validates the computational approach. Slight
366 deviations are attributable to inherent DFT approximations and excitonic effects in the solid
367 state. Overall, these findings underscore that a careful balance of backbone planarity, donor–
368 acceptor segmentation, and electron-rich bridging motifs can be harnessed to fine-tune
369 HOMO–LUMO energy levels, thereby enhancing both charge transport and device
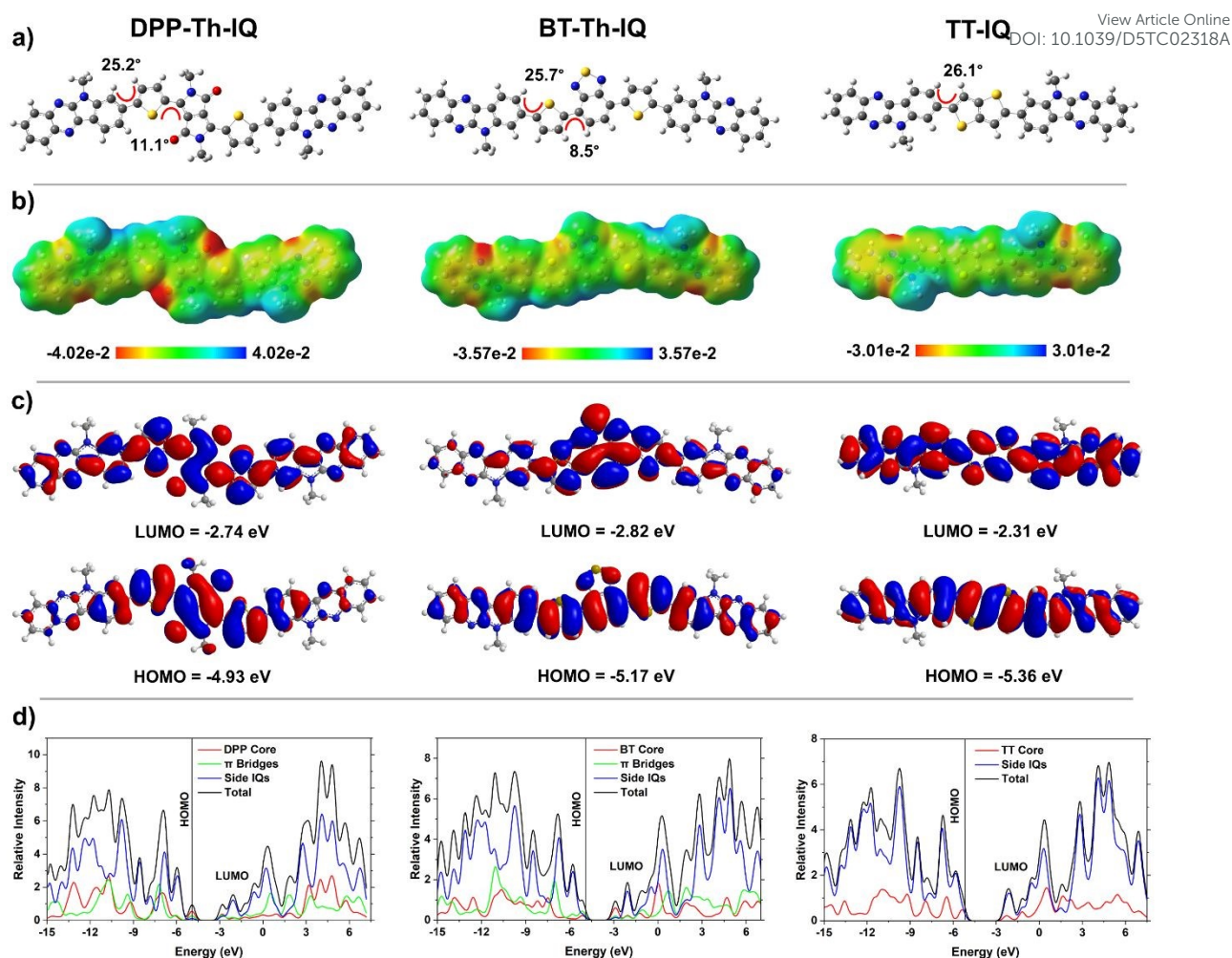370 performance in OSCs.

Figure 2. (a) Optimized molecular geometries, (b) molecular electrostatic potential (MESP) surfaces, (c) frontier molecular orbitals delocalization, and (d) partial DOS (PDOS) graphs based on core, bridging, and end-capped fragments in the SMDs simulated by B3LYP/6-31G (d,p) method.

Optical Properties and Solvatochromism

Optical characteristics of synthesized SMDs were evaluated to assess their suitability in OSCs. **Table 3** summarizes the experimental absorption and emission spectral characteristics, along with respective theoretical parameters derived from TD-DFT calculations. Steady state optical spectroscopy was employed to examine the SMDs in dilute chloroform solutions (2.5 µg/mL). The UV-Vis spectra of the representative samples are shown in **Figure 3a**, with the absorption covering the spectral range of 500nm, 570nm and 740nm. The latter sample exhibited extended absorption and broader spectrum compared to its counterparts. Whilst TT-IQ yielded an absorption peak value at 435 nm, BT-Th-IQ displayed absorption peaks at 386 nm and 480 nm.

DPP-Th-IQ exhibited the most red-shifted absorption maxima (λ_{max}^{abs}) in solution at 630 nm with an additional peak at 400 nm. The 630 nm peak reflects significant ICT attributed to its DPP core and extended conjugation through bridging thiophenes. By contrast, λ_{max}^{abs} in thin-film revealed a notable red shift to 710 nm, indicative of altered intermolecular interactions or π-π stacking in the solid state as shown in **Figure 3c**. Whereas BT-Th-IQ SMD showed a most pronounced gap between its solution λ_{max}^{abs} 386 nm and thin-film λ_{max}^{abs} at 515 nm, underscoring the strongest influence of molecular packing on these materials.

391   The PL spectra of the SMDs were measured in dilute chloroform solutions and given in **Figure**
392   **3b**. DPP-Th-IQ exhibited the most red-shifted emissions maxima λ_{max}^{emi} at 664 nm due to
393   enhanced ICT.[46] Whereas, BT-Th-IQ and TT-IQ showed consistent emission maxima at 493
394   nm and 495nm respectively. In **Table 2** we further show the respective Stokes shifts (λst) for
395   the SMDs calculated based on λ_{max}^{abs} and λ_{max}^{emi} differences. A relatively small λst of 34 nm in
396   DPP-Th-IQ suggests minimal structural rearrangement in the excited state which is indicative
397   that the chromophore can reduce the non-radiative energy losses and favor higher photocurrent
398   generation.[47-50] Whereas, the large λst of 107 nm suggests a substantial reorganization of the
399   BT-Th-IQ framework upon photoexcitation, which may offer avenues for exciton
400   management. Meanwhile, TT-IQ SMD, featuring a TT core having λ_{max}^{abs} at 435 nm and λ_{max}^{emi}
401   at 495 nm in chloroform with respective λst of 60 nm has a lower spectral coverage, suggesting
402   that strategic combination with complementary acceptors could exploit TT-IQ's slightly higher
403   energy gap to maximize overall solar absorption. The photoexcitation-states based charge
404   transfer is further discussed in the subsequent sections.

405   Solvatochromic effect was investigated by recording UV-Vis absorption and
406   photoluminescence spectra in chlorobenzene, tetrahydrofuran, toluene, and methanol. The
407   spectra are given in Supporting Information **Figure S11** and detailed in **Tables S2-S4**. Among
408   the synthesized SMDs, DPP-Th-IQ displayed the largest bathochromic response, with λ_{max}^{abs}
409   shifting from 598-610 nm in non-polar media to 660 nm in methanol and λ_{max}^{emi} red-shifting
410   from 660-665 nm to 800 nm with $\lambda st \approx 140$ nm. The pronounced shift highlights strong ICT
411   stabilization in polar environments.[51-52] BT-Th-IQ showed smaller absorption changes, such as
412   from 380-387 nm to ~513 nm in methanol. Yet a sizable PL red-shift, which resulted in λst in
413   the range 92–133 nm, indicated the polarity-induced excited-state reorganization. Whereas,
414   TT-IQ SMD exhibited minimal solvent-dependent shifts in λ_{max}^{abs} (425–430 nm), yet its λ_{max}^{emi}
415   exhibited considerable sensitivity, shifting from 485–490 nm in nonpolar solvents to 550 nm
416   in methanol. This resulted in a significant increase in λst from about 57–65 nm in lower
417   polarity solvents to up to 121 nm in highly polar methanol. The combined trends confirm that
418   solvent polarity predominantly tunes excited-state relaxation, with DPP-Th-IQ experiencing
419   the greatest ICT-driven stabilization.

420   Additionally, the TD-DFT simulations with CAM-B3LYP/6-31G(d,p) method were carried out
421   and given in **Table 2**. Computational results support the experimental findings by predicting
422   λ_{theo}^{abs} values that mirror the observed red-blue absorption trends. Specifically, DPP-Th-IQ and
423   BT-Th-IQ reveal relatively low-energy electronic transitions at 543 nm and 503 nm,
424   respectively, while TT-IQ appears more blue-shifted at 388 nm. The $S_0–S_1$ excitation energy
425   (E_X), transition dipole moment (μ_{tr}), and oscillator strength (f) offer additional insights into
426   each SMD's propensity for strong light absorption and effective exciton generation which is a
427   critical parameter for high photocurrent in OSC. Notably, TT-IQ exhibits the largest μ_{tr} (38.5
428   a.u.) and highest f (2.85), underscoring a particularly intense transition. Molecular orbitals
429   configuration interaction (C.I.) analyses further confirmed that these prominent absorptions
430   arise primarily from the HOMO → LUMO transitions, supplemented by minor contributions
431   from nearby orbitals such as HOMO → LUMO+2 in DPP-Th-IQ and HOMO-4 → LUMO in
432   BT-Th-IQ. Overall, these photophysical characteristics highlight the importance of structural
433   tuning in SMDs. DPP-Th-IQ leverages a strongly red-shifted profile that can capture lower-
434   energy photons, BT-Th-IQ gains considerable absorption enhancement in the solid state, and
435   TT-IQ offers robust transition strengths and moderate film-phase shifts.

436   Based on the above experimental and computational optoelectronic analysis, the synthesized
437   SMDs showcase varied trends in molecular interactions, processing conditions, and CT

438 behavior. For instance, the DPP-Th-IQ SMD, with its highly sensitive ICT response and red-
439 shifted absorption, suggests strong D/A interactions in BHJ blends. Its ability to maintain broad
440 absorption in various solvent environments makes it an excellent candidate for low-bandgap
441 OSCs. BT-Th-IQ, showing high film-phase aggregation and moderate solvatochromic effects,
442 suggests potential as a highly tunable donor, where solvent engineering can be leveraged to
443 optimize film morphology and charge mobility. TT-IQ, with high oscillator strength and
444 moderate solvatochromic shifts, could serve as a complementary donor in multi-component
445 blends, where its higher transition dipole moment may enhance CT at D/A interfaces.

446 **Table 2.** Optical characteristics of the synthesized DPP-Th-IQ, BT-Th-IQ, and TT-IQ SMDs.

Molecule	Experimental				Theoretical				C.I.[e]
	$\lambda^{abs}_{sol.}$ (nm)[a]	$\lambda^{abs}_{fil.}$ (nm)[a]	$\lambda^{emi}_{sol.}$ (nm)[a]	λst (nm)[b]	$\lambda^{abs}_{theo.}$ (nm)[c]	E_X (eV)[d]	μ_{tr} (a.u.)[d]	f[d]	
DPP-Th-IQ	630	710	664	34	543	2.27	28.1	1.57	H→L (+68%)
									H→L+2 (+11%)
BT-Th-IQ	386	515	493	107	503	2.46	31.5	1.87	H→L (+67%)
									H-4→L (+10%)
TT-IQ	435	460	495	60	388	3.19	38.5	2.85	H→L (+63%)
									H-3→L+1 (+20%)

447 [a]Wavelengths of the absorption/emission maxima ($\lambda^{abs}_{sol.}/\lambda^{emi}_{sol.}$) in Chloroform solutions (2.5 μg /mL)
448 and in film ($\lambda^{emi}_{fil.}$) at wavelengths of 410 nm; [b]Stokes shift (λst) calculated from absorption and
449 emission maxima difference; [c]Theoretically calculated absorption maxima ($\lambda^{abs}_{theo.}$); [d]S_0-S_1 state
450 excitation energy (E_X), transition electric dipole moment (μ_{tr}), and oscillatory strength (f); [e]Orbitals
451 charge transfer configuration interactions (C.I.), simulated by TD-DFT/CAM-B3LYP/6-31G (d,p)
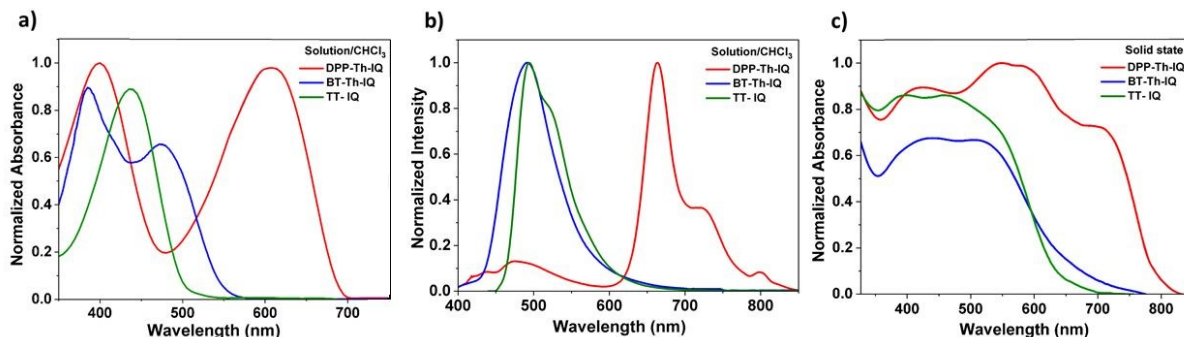452 method.

454 **Figure 3.** (a) Normalized absorption (b) normalized emission spectra upon optical excitation at 390
455 nm, 415 nm and 385 nm for DPP-Th-IQ, BT-Th-IQ and TT-IQ respectively in Chloroform (2.5
456 μg/mL) solution (c) thin-films absorption spectra profile of the synthesized SMDs.

457 **Thermal and Photostability**

458 The photostability of the IQ-based SMDs was assessed in the thin-film state. Thin films were
459 prepared by spin-coating (0.1 mg mL⁻¹) chlorobenzene solutions onto pre-cleaned quartz
460 substrates (1 × 1 cm²) at 2000 rpm for 60 s, followed by thermal annealing at 100 °C for
461 20 minutes under vacuum to remove residual solvent and enhance molecular ordering. The
462 films were then exposed to continuous AM 1.5G solar irradiation (100 mW cm⁻²) for 30 h
463 under ambient conditions. Photo degradation was monitored by UV-Vis absorption
464 spectroscopy at regular intervals. The evolution of normalized absorbance over time is
465 presented in Supporting Information **Figure S13 a-c**, with comparative stability data

466 summarized in **Table S5**. All SMDs demonstrated excellent photo stability up to 90% retained
467 absorbance after exposure for 30 hrs.

468 To investigate thermal behavior and molecular interactions, temperature-dependent UV-Vis
469 absorption measurements were conducted in chlorobenzene (0.1 mg mL⁻¹) over the range of
470 20 °C to 120 °C. Spectra are shown in Supporting Information **Figure S13 d-f**. DPP-Th-IQ and
471 BT-Th-IQ showed minimal bathochromic shifts and modest intensity changes with temperature
472 which indicates stable π–π interactions/aggregation states that persist upon heating. In contrast,
473 TT-IQ displayed more noticeable intensity variations at elevated temperature, pointing to
474 comparatively weaker intermolecular interactions. Thermal stability was further evaluated by
475 TGA under nitrogen atmosphere at a heating rate of 10 °C min⁻¹. As shown in the TGA profiles
476 in Supporting Information **Figure S14**, the 5% mass-loss temperatures ($T_5\%$) exceeded 250 °C
477 for all SMDs and were highest for BT-Th-IQ ~410 °C and DPP-Th-IQ ~400 °C, with TT-IQ
478 the lowest ~270 °C. The high decomposition thresholds of DPP-Th-IQ and BT-Th-IQ define
479 comfortable processing windows and support their robustness during solution deposition and
480 post-deposition annealing.

481 **Reorganization Energy and Solvation Free Energy**

482 Charge transport in OSCs is governed by the ability of the donor and acceptor molecules to
483 efficiently facilitate charge hopping. This efficiency is quantified by the reorganization energy,
484 which represents the energy associated with structural relaxation upon CT.[53-54] Herein, λ_{hole}
485 and λ_{ele} were calculated for the SMDs and the Y6 NFA via B3LYP/6-31G(d,p) method to
486 determine hole and electron mobility, respectively. The results are summarized in **Table 3**.

487 Among the SMDs, BT-Th-IQ exhibited the lowest λ_{hole} (0.255 eV), followed closely by TT-IQ
488 (0.258 eV), and DPP-Th-IQ (0.288 eV). The relatively low λ_{hole} of BT-Th-IQ suggests that it
489 possesses the most favorable hole transport properties among the three donors, as a lower hole
490 reorganization energy reduces charge-trapping losses and enhances carrier mobility. The BT
491 core likely contributes to this reduced reorganization energy by minimizing geometric
492 relaxation upon oxidation, leading to more efficient hole transport. In contrast, DPP-Th-IQ
493 exhibited the highest λ_{hole} (0.288 eV), suggesting that it experiences greater structural distortion
494 upon hole injection, potentially due to localized charge distribution in the oxidized state. For
495 electron transport, DPP-Th-IQ exhibited the lowest λ_{elec} (0.213 eV), which is favorable for
496 robust electron transport due to the electron-deficient nature of the DPP core, which stabilizes
497 the negative charge upon reduction and reduces the structural reorganization for CT. On the
498 other hand, BT-Th-IQ and TT-IQ have slightly higher λ_{ele} (0.237 eV and 0.241 eV,
499 respectively), indicating marginally less electron transport efficiency than DPP-Th-IQ.
500 Moreover, for efficient charge separation and transport in photoactive layer, the reorganization
501 energies of donors and acceptors should be well balanced.[55-56] The benchmark NFA Y6
502 exhibits significantly lower λ_{hole} (0.160 eV) and λ_{ele} (0.150 eV), reinforcing its role as an
503 efficient charge transporter. The lower reorganization energy of Y6 confirms that it can readily
504 accept electrons from SMDs, minimizing energy loss during charge separation and facilitating
505 long-lived charge carriers in photoactive layer. Comparatively the SMDs have higher λ_{hole}
506 values than Y6, suggesting that hole transport is slightly less efficient than electron transport.
507 However, the relatively small gap between λ_{hole} and λ_{ele} in the three SMDs suggests that these
508 molecules can still achieve balanced charge transport, an important factor in reducing charge
509 recombination and increasing FF in OSCs. These results show that the IQ-capped molecules
510 are excellent candidates for high-performance OSCs, particularly when paired with low-
511 reorganization-energy acceptors like Y6.

512 Additionally, the molecular polarity, charge redistribution, and solubility are the other key
513 parameters which are influenced by the dipole moment and solvation free energy and greatly
514 affect film morphology and charge transport in OSCs.[43, 57] Herein, the dipole moment and
515 Gibbs solvation-free energy (ΔG_{solv}) were further computed via M06-2X/6-31G (d,p) method
516 in chloroform solvent. Results given in **Table 3** show that among SMDs, BT-Th-IQ exhibited
517 the highest ground-state dipole moment (μ_g = 3.43 D) and excited-state dipole moment (μ_e =
518 4.47 D), with the largest dipole moment variation ($\Delta\mu$ = 1.04 D). This indicates strong charge
519 redistribution upon excitation, consistent with its high CT character. DPP-Th-IQ and TT-IQ
520 exhibited lower dipole moment variation ($\Delta\mu$ = 0.67 D), suggesting moderate ICT
521 contributions, while Y6 displays a dipole moment variation ($\Delta\mu$ = 0.82 D), indicating a
522 moderate degree of charge separation. Whereas, DPP-Th-IQ exhibited the most negative ΔG_{solv}
523 (-40.84 kcal/mol), followed by BT-Th-IQ (-37.94 kcal/mol) and TT-IQ (-31.92 kcal/mol),
524 indicating that DPP-Th-IQ has the highest solubility in chloroform, which may aid in better
525 thin-film formation.

526 **Table 3.** Hole/electron reorganization energy ($\lambda_{hole}/\lambda_{ele}$) calculated by B3LYP/6-31G (d,p) method and
527 dipole moment in ground-state (μ_g) and excited-state (μ_e) with respective Gibbs solvation-free energy
528 (ΔG_{solv}) in chloroform solvent calculated using M06-2X/6-31G (d,p) method via SMD solvation model.

Molecule	λ_{hole} (eV)	λ_{ele} (eV)	μ_g (Debye)	μ_e (Debye)	$\Delta\mu$ (Debye)	ΔG_{solv} (kcal/mol)
DPP-Th-IQ	0.288	0.213	2.55	3.22	0.67	-40.84
BT-Th-IQ	0.255	0.237	3.43	4.47	1.04	-37.94
TT-IQ	0.258	0.241	2.44	3.09	0.67	-31.92
Y6	0.160	0.150	1.07	1.89	0.82	-14.61

Intramolecular Charge Transfer and Transition Density Analysis

531 ICT and exciton dissociation play a pivotal role in the performance of the OSCs.[54] To
532 comprehend the photoexcitation dynamics of the synthesized SMDs, a detailed electron
533 transition density analysis was performed based on TD-DFT/CAM-B3LYP/6-31G (d,p)
534 calculations in MultiWfn 3.8. The analysis includes key electron transition properties such as
535 CT distance (D_{CT}), H_{index}, t_{index}, intrinsic CT excitation, intrinsic local excitation (LE),
536 transferred charge *(q_{CT})*, hole/electron delocalization indices (HDI/EDI), and exciton binding
537 energy (E_B), as summarized in **Table 4**.[21, 29] To visualize the charge distribution, electron
538 density difference (EDD) contours, hole/electron heat maps, and transition density matrix
539 (TDM) heat maps were also generated and given in **Figure 4**.

540 As shown in the EDD graphs showcasing holes (cyan) and electrons (blue) delocalization
541 in **Figure 4a** and respective heat maps in **Figure 4b**, the holes (59.1%) and electrons (50.8%)
542 are predominantly localized on the DPP core, with moderate contributions from the thiophene
543 bridges (29.5% for holes, 36.5% for electrons) and minimal distribution in the side IQ units
544 (11.4% for holes, 12.6% for electrons) in DPP-Th-IQ SMD. This suggests strong electronic
545 coupling between the DPP core and thiophene bridges, which enhances charge delocalization.
546 In BT-Th-IQ, electrons are mostly concentrated on the BT core (66.2%), whereas holes are
547 mainly distributed over the thiophene bridges (51.4%), indicating a well-defined charge-
548 separated state that facilitates charge extraction. In TT-IQ, holes (46.7%) and electrons (34.1%)
549 are more evenly distributed across the molecular skeleton, particularly between the TT core
550 and IQ end-groups. This widespread delocalization enhances charge transport but may also
551 increase hole/electron recombination. TDM heat maps in **Figure 4c** further illustrate the extent
552 of hole/electron spatial overlap within different molecular segments. Regular hole and electron
553 generation patterns observed across all three SMDs indicate efficient charge separation,
554 particularly in BT-Th-IQ and DPP-Th-IQ. These findings suggest that all three donors

555 exhibited well-defined ICT characteristics, which are favorable for charge transport and
556 exciton dissociation in OSCs.

557 D_{CT} provides a measure of the spatial charge separation in the excited state, influencing exciton
558 dissociation efficiency. Among the three SMDs, BT-Th-IQ exhibited the largest D_{CT} (0.87 Å),
559 followed by TT-IQ (0.11 Å) and DPP-Th-IQ (0.06 Å), indicating that BT-Th-IQ exhibits the
560 most significant charge separation upon photoexcitation. A higher D_{CT} value suggests stronger
561 charge separation, which is beneficial for reducing recombination and promoting efficient
562 charge extraction in OSCs. Conversely, DPP-Th-IQ shows a lower D_{CT}, suggesting a more
563 localized excitonic state. CT and LE components further characterize the nature of the
564 electronic transitions. BT-Th-IQ exhibits the highest CT contribution (65.2%), indicating a
565 highly polarized charge distribution that favors efficient charge transfer. In comparison, DPP-
566 Th-IQ (57.7%) and TT-IQ (48.9%) exhibit lower CT contributions, with TT-IQ displaying the
567 highest LE component (51.1%), suggesting a more localized charge distribution. These
568 findings confirm that BT-Th-IQ is the most promising donor for achieving long-range charge
569 separation, while TT-IQ, with its higher LE component, may rely more on intermolecular
570 interactions to facilitate charge transport.

571 The parameter q_{CT} further provides quantitative measure of charge redistribution in the excited
572 state. From the results, BT-Th-IQ exhibited the highest q_{CT} (0.48 e$^-$), followed by TT-IQ (0.43
573 e$^-$) and DPP-Th-IQ (0.38 e$^-$). The larger q_{CT} of BT-Th-IQ confirms strong ICT behavior,
574 which is beneficial for reducing energy loss during charge transport. HDI and EDI further
575 indicate the extent of charge delocalization across the molecular framework. DPP-Th-IQ SMD
576 having HDI/EDI of 5.78/5.68 and BT-Th-IQ with HDI/EDI 5.00/5.70 exhibited widespread
577 charge delocalization, facilitating charge hopping and improving charge mobility. Whereas,
578 TT-IQ, with lower HDI/EDI of 4.83/4.20, suggests a more localized charge transport pathway.
579 Furthermore, the BT-Th-IQ SMD exhibited the lowest E_B (0.31 eV), followed by DPP-Th-IQ
580 (0.41 eV) and TT-IQ (0.44 eV). The reduced E_B in BT-Th-IQ is attributed to its high CT
581 character and significant charge transfer distance, further reinforcing its higher charge transport
582 characteristics. The slightly higher E_B in TT-IQ suggests a more tightly bound excitonic state,
583 which may require an optimized D/A interface to enhance charge dissociation.

584 **Table 4.** Electron transition density properties of the designed SMDs including charge transfer distance
585 (D_{CT}), H_{index}, t_{index}, intrinsic charge transfer (CT) excitation, intrinsic local excitation (LE), transferred
586 charge (q_{CT}), hole/electron delocalization index (HDI/EDI), and exciton binding energy (E_B) simulated
587 by TD-DFT/CAM-B3LYP method.

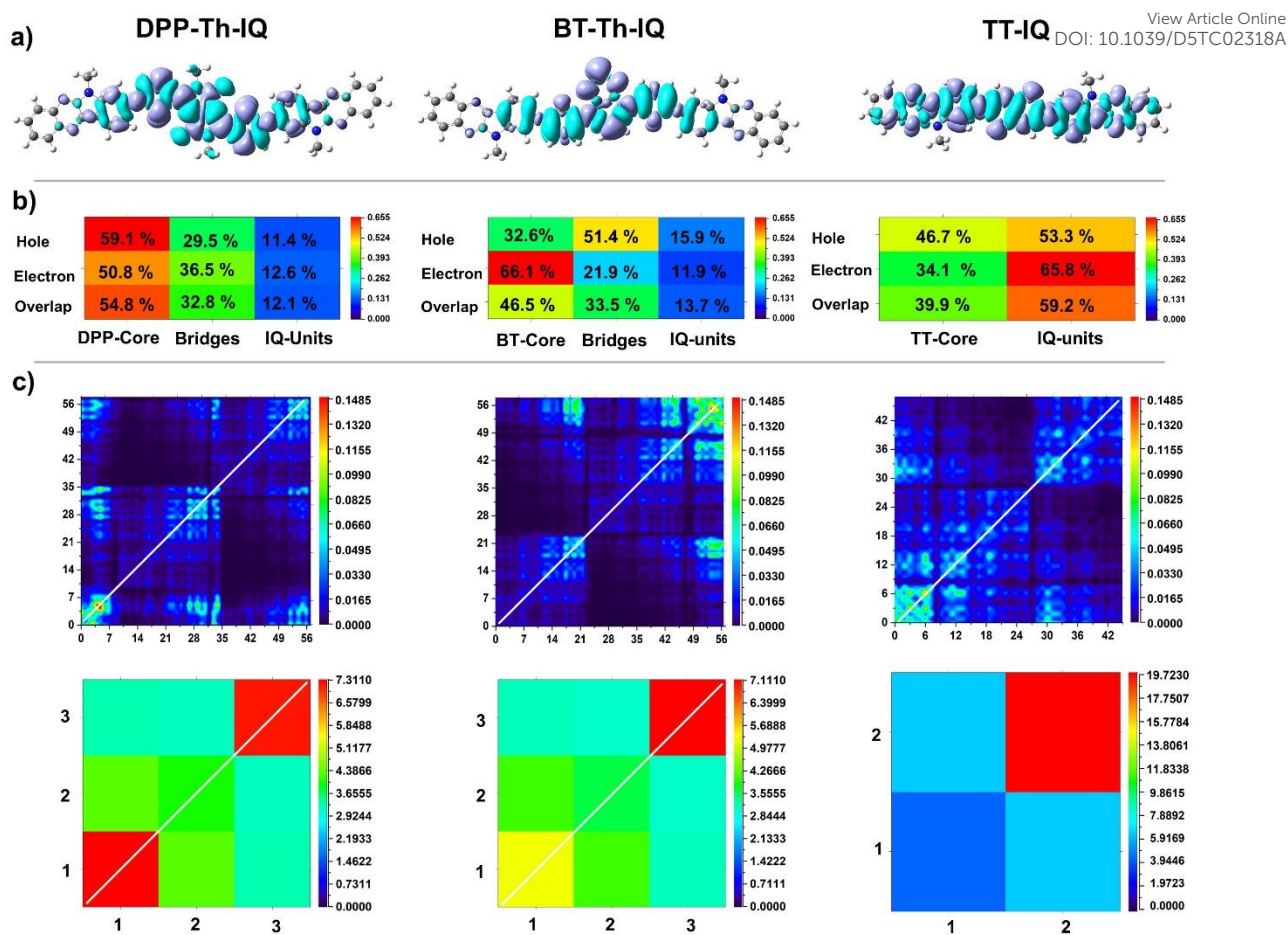| Molecule	D_{CT} (Å)	H_{index} (Å)	t_{index} (Å)	CT (%)	q_{CT} (e$^-$)	LE (%)	HDI	EDI	E_B (eV)
DPP-Th-IQ	0.06	4.59	-0.88	57.75	0.38	42.25	5.78	5.68	0.41
BT-Th-IQ	0.87	4.84	-0.98	65.22	0.48	34.77	5.00	5.70	0.31
TT-IQ	0.11	6.18	-076	48.95	0.43	51.05	4.83	4.20	0.44

Figure 4. (a) Electron density difference (EDD) surface contours, (b) hole/electron heat maps with percentage delocalization and spatial overlap within core units, thiophene bridges, and end-group IQs, (c) and transition density matrix (TDM) heat maps for atoms and molecular fragments such as core units (1), thiophene bridges (2), and side IQs units (3), simulated via TD-DFT/CAM-B3LYP method.

Donor/Acceptor Interfacial Charge Transfer Properties

Efficient interfacial CT at the D/A interface plays a pivotal role in determining the performance of OSCs, as it critically affects CT state dissociation and free-charge generation.[58] To explore CT characteristics, the interfacial packing, excited-state configurations, and CT mechanisms of complexes formed between the synthesized SMDs and the benchmark Y6 NFA were studied. Initially, optimized face-on orientation configurations of D/A complexes were constructed with an initial donor–acceptor separation of 3.5 Å. Geometry optimization was carried out at the B3LYP/6-31G (d,p) level, followed by TD-DFT calculations with the RSH functional CAM-B3LYP and the CT analysis based on EDD method via MultiWfn 3.8.[59-60]

The optimized D/A complex geometries given in **Figure 5a–b**, demonstrated distinct intermolecular arrangements for each donor when combined with Y6. All three complexes DPP-Th-IQ/Y6, BT-Th-IQ/Y6, and TT-IQ/Y6 exhibited a preferred face-on π–π stacking orientation, facilitating strong intermolecular electronic interactions. Notably, the TT-IQ/Y6 complex displayed the largest intermolecular π–π stacking area, indicative of extensive D/A interfacial overlap. However, despite the smaller stacking areas, the DPP-Th-IQ/Y6 and BT-Th-IQ/Y6 complexes exhibit significantly shorter centroid-to-centroid distances of 5.13 Å and 5.22 Å, respectively, compared to TT-IQ/Y6 at 6.27 Å. These shorter distances imply stronger intermolecular interactions and closer packing arrangements driven by the favorable electronic

611 coupling of the DPP and BT cores with Y6. Further structural dimensions were measured to
612 analyze the molecular packing in D/A complexes. As shown in **Figure 5c**, the lengths of the
613 DPP-Th-IQ/Y6, BT-Th-IQ/Y6, and TT-IQ/Y6 complexes are 33.9 Å, 34.8 Å, and 29.7 Å,
614 respectively, with widths of 17.8 Å, 17.6 Å, and 16.3 Å, and heights of 11.7 Å, 10.1 Å, and 8.1
615 Å, respectively. Side-view packing configurations and dimensional data revealed well-defined
616 and stable intermolecular stacking patterns as characterized by parallel alignment and slightly
617 curved "half-bowl" conformations.

618 Excited-state vertical transitions and interfacial CT behaviors for the lowest three excited states
619 (S_1–S_3) were thoroughly evaluated for the D/A complexes and described in **Figure 5d**. The
620 EDD method allows clear visualization of electron transition processes as "hole→electron"
621 distributions, categorizing excited states into Frenkel excitons (localized) and pure/hybrid CT
622 states (electron and hole spatially separated across donor and acceptor). For the DPP-Th-IQ/Y6
623 complex, the lowest-energy excited state (S_1 at 2.11 eV, f=1.2) shows moderate charge transfer
624 (CT≈18%, q_{CT}=0.53 e$^-$, D_{index} =2.88 Å), predominantly acceptor-localized with ≈90%
625 hole/electron localization on Y6. However, higher-energy states such as S_2 (2.35 eV, 56% CT,
626 4.73 Å D_{index}) and S_3 (2.56 eV, 46% CT, 4.36 Å D_{index}) exhibit increased charge separation,
627 suggesting an enhanced likelihood of exciton dissociation at elevated excitation energies. EDD
628 contours confirm this, demonstrating progressively stronger donor-involved CT contributions
629 at these higher states. In contrast, the S_1 excitation in TT-IQ/Y6 at 2.18 and subsequent excited
630 state S_2 at 2.60 eV shows minimal charge separation (0-2.5% CT), indicating the presence of
631 localized Frenkel-type excitations at lowest and intermediate states. However, the third excited
632 state S_3 at 3.0 eV recovers robust CT characteristics (97% CT, q_{CT}=0.94 e$^-$, D_{index}=4.63 Å).
633 These findings confirm that TT-IQ/Y6 also presents suitable excited-state charge-transfer
634 dynamics conducive to efficient exciton dissociation.

635 Overall, the interfacial mechanistic analysis suggests that among the modelled SMDs/Y6
636 complexes, BT-Th-IQ/Y6 exhibits the high CT percentages, substantial transferred charges,
637 and significant spatial electron-hole separation distances, all beneficial for promoting efficient
638 CT state dissociation and charge generation. DPP-Th-IQ/Y6, despite its smaller π–π stacking
639 distance, efficiently achieves notable CT character and robust excited-state interactions.
640 Whereas, the TT-IQ/Y6 complex, with broader π–π stacking and moderate interfacial CT
641 distances, also demonstrates effective charge separation dynamics. Thus, all three donor
642 complexes demonstrate favorable excited-state and structural characteristics at the molecular
643 interface with the Y6 acceptor, highlighting their potential in the design and fabrication of
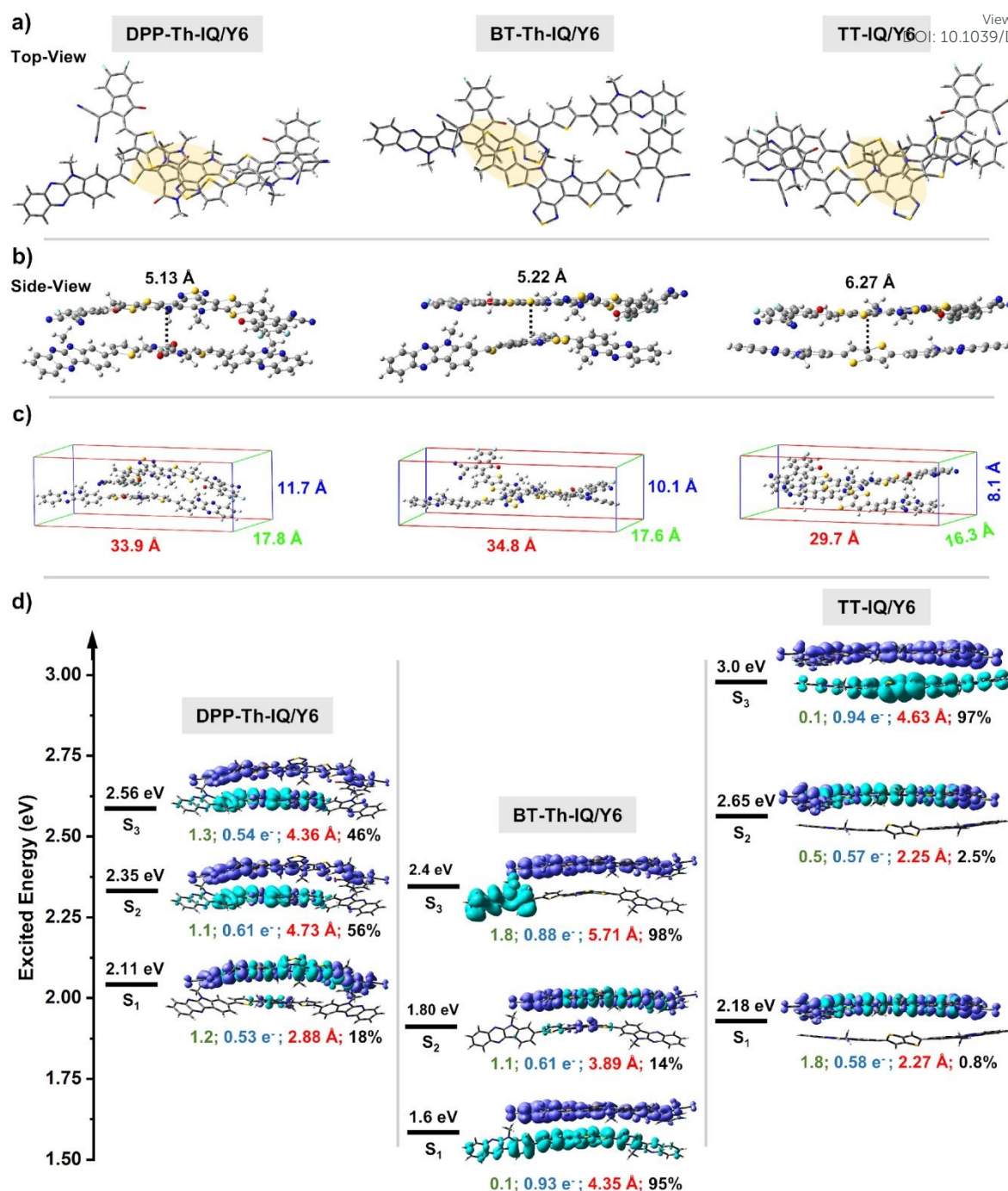644 future ASM-OSCs.

Figure 5. (a) and (b) Top and side views of the optimized face-on D/A complexes (DPP-Th-IQ/Y6, BT-Th-IQ/Y6, and TT-IQ/Y6) obtained at the DFT/B3LYP/6-31G(d,p) level, illustrating the π–π stacking orientation and centroid-to-centroid distances. (c) Dimensional analysis of length, width, and height of each simulated D/A complex. (d) Low-lying excited-state properties (S_1–S_3) derived from TD-DFT/CAM-B3LYP/6-31G (d,p) calculations based on EDD method, highlighting excitation energies, oscillator strengths (green), transferred charge (blue), charge transfer distance index (red), and CT excitation percentages (black) for each donor/Y6 complex and their respective EDD isosurfaces.

4. Conclusions

In this work, three SMDs named DPP-Th-IQ, BT-Th-IQ, and TT-IQ, were successfully designed, synthesized, and characterized for potential application in next-generation ASM-

657 OSCs. Incorporating easily synthesized IQ-terminal moieties, combined with electron-
658 deficient diketopyrrolopyrrole and benzothiadiazole cores, as well as an electron-rich
659 thienothiophene core, we systematically explored the impact of structural motifs on their
660 electronic, optical, charge transport, interfacial charge transfer properties and molecular
661 stability. The strategically designed SMDs featuring a streamlined cost-efficient synthesis is
662 beneficial for scalability, paving the way for potential commercial applications in future ASM-
663 OSCs.

664 Electrochemical and DFT calculations revealed well-matched HOMO–LUMO offsets with the
665 Y6 acceptor, indicating sufficient driving force for exciton dissociation into free charges.
666 Notably, DPP-Th-IQ exhibited significantly improved optical properties, including redshift in
667 λ_{max}^{abs} (630 nm) and λ_{emi}^{abs} (664 nm), the smallest electrochemical bandgap (1.65 eV), offering
668 extended absorption in the visible–near-infrared range, in addition to improved solvation
669 properties (ΔG_{solv} = -40.84 kcal/mol), which can facilitate solution-processing and film
670 formation. Moreover, the lowest electron reorganization energy (0.213 eV)) of DPP-Th-IQ,
671 highlighting its capacity for swift electron transfer. Meanwhile, BT-Th-IQ demonstrated the
672 highest charge transfer character (CT = 65.22%) and the longest charge transfer distance (D_{CT}
673 = 0.87 Å), accompanied with the lowest exciton binding energy (0.31 eV) and low hole
674 reorganization energy (0.255 eV) for improved hole mobility positioning it as the most
675 promising donor for long-range charge separation. Moreover BT-Th-IQ showed a notable red
676 shift in thin film (386 nm-515 nm) reflecting film-phase interactions to effective charge
677 transport, while TT-IQ exhibited balanced hole/electron delocalization, making it a useful
678 complementary donor in OSC architectures. Whereas, the interfacial analysis of optimized
679 donor/Y6 complexes demonstrated stable face-on π–π stacking configurations with robust D/A
680 interactions. BT-Th-IQ/Y6 complex yielded efficient CT states, underpinning their potential
681 for high J_{SC}. DPP-Th-IQ/Y6 complex showed enhanced interfacial CT indicating favorable
682 structural attributes for achieving high charge transport mobilities. Although TT-IQ/Y6
683 demonstrated extensive interfacial stacking, its variable CT efficiency across excitation
684 energies highlighted the need for precise morphological optimization to ensure consistent
685 device performance. Importantly, the materials exhibited encouraging durability. Thin films
686 retained ≥ 90% of their initial absorbance after 30 h of continuous AM 1.5G irradiation (100
687 mW cm⁻²), evidencing good photo-stability under operationally relevant conditions.
688 Thermogravimetric analysis indicates $T_{d, 5\%}$ > 250 °C for all donors, underscoring robust
689 thermal stability.

690 Overall, our findings provide valuable molecular-design insights. Among the three donors,
691 BT-Th-IQ showed the highest intrinsic charge-separation fraction, lowest exciton-binding
692 energy, and the most balanced hole/electron reorganization energies, together with robust
693 face-on π–π stacking with Y6. These traits favor efficient CT state dissociation and balanced
694 carrier transport. DPP-Th-IQ and TT-IQ exhibited complementary strengths, such as deeper
695 HOMO for higher V_{OC} and symmetric hole delocalization. The present work therefore
696 establishes a detailed atomistic structure-property framework that sets critical benchmarks for
697 subsequent optimization. Full photovoltaic device fabrication and characterization (V_{OC}, J_{SC},
698 fill factor and PCE measurements) are proposed as the logical next step to realize the
699 performance potential of these IQ-capped small-molecule donors in all-small-molecule OSC
700 architectures.

Conflicts of interest

701

702 There are no conflicts to declare.

Supporting Information

File SI: Detailed experimental procedures for the synthesis of the new SMDs, including characterization data and simulation results supporting the findings in the main manuscript.

Acknowledgements

Credit authorship contribution statement

Maryam Javed: Synthesis, Purification, Experimental characterization, Formal analysis, Investigation, Writing – original draft. **Waqas Akram:** Synthesis, Experimental characterization, Computational methodology, Formal Analysis, Data curation, Visualization, Investigation, Writing – original draft. **Zeeshan Ali:** Experimental methodology, Synthesis, Characterization. **Nabeel Shahzad:** Software, Computational analysis, Data curation, Visualization. **Munazza Shahid:** Conceptualization, Writing – review & editing. **Ghayoor Abbas Chotana:** Resources, Software, Methodology. **Jafar Iqbal Khan:** Methodology, Validation, Writing – review & editing. **Jie Min:** Data curation, Validation, Resources. **Muhammad Altaf:** Methodology, Validation, Data curation. **Christian B. Nielsen:** Methodology, Writing – review & editing. **Raja Shahid Ashraf:** Conceptualization, Supervision, Resources, Methodology, Funding accusation, Project administration.

References:

1.	Karunakaran, S. K.; Arumugam, G. M.; Yang, W.; Ge, S.; Khan, S. N.; Lin, X.; Yang, G., Recent progress in inkjet-printed solar cells. *Journal of Materials Chemistry A* **2019,** *7* (23), 13873-13902.

2.	Tsang, M. P.; Sonnemann, G. W.; Bassani, D. M., Life-cycle assessment of cradle-to-grave opportunities and environmental impacts of organic photovoltaic solar panels compared to conventional technologies. *Solar Energy Materials and Solar Cells* **2016,** *156*, 37-48.

3.	Lipomi, D. J., Organic photovoltaics: focus on its strengths. *Joule* **2018,** *2* (2), 195-198.

4.	Zhao, J.; Li, Y.; Yang, G.; Jiang, K.; Lin, H.; Ade, H.; Ma, W.; Yan, H., Efficient organic solar cells processed from hydrocarbon solvents. *Nature Energy* **2016,** *1* (2), 1-7.

5.	Ganesamoorthy, R.; Sathiyan, G.; Sakthivel, P., Fullerene based acceptors for efficient bulk heterojunction organic solar cell applications. *Solar Energy Materials and Solar Cells* **2017,** *161*, 102-148.

6.	Li, C.; Song, J.; Lai, H.; Zhang, H.; Zhou, R.; Xu, J.; Huang, H.; Liu, L.; Gao, J.; Li, Y., Non-fullerene acceptors with high crystallinity and photoluminescence quantum yield enable> 20% efficiency organic solar cells. *Nature Materials* **2025**, 1-11.

7.	Liu, Q.; Jiang, Y.; Jin, K.; Qin, J.; Xu, J.; Li, W.; Xiong, J.; Liu, J.; Xiao, Z.; Sun, K., 18% Efficiency organic solar cells. *Science Bulletin* **2020,** *65* (4), 272-275.

8.	Kan, B.; Kan, Y.; Zuo, L.; Shi, X.; Gao, K., Recent progress on all-small molecule organic solar cells using small-molecule nonfullerene acceptors. *InfoMat* **2021,** *3* (2), 175-200.

9.	Gao, H.; Sun, Y.; Meng, L.; Han, C.; Wan, X.; Chen, Y., Recent progress in all-small-molecule organic solar cells. *Small* **2023,** *19* (3), 2205594.

10.	Liu, Y.; Wan, X.; Wang, F.; Zhou, J.; Long, G.; Tian, J.; Chen, Y., High-performance solar cells using a solution-processed small molecule containing benzodithiophene unit. *Advanced Materials* **2011,** *23* (45), 5387-5391.

11.   Zhou, J.; Wan, X.; Liu, Y.; Zuo, Y.; Li, Z.; He, G.; Long, G.; Ni, W.; Li, C.; Su, X.; Chen, Y., Small molecules based on benzo[1,2-b:4,5-b′]dithiophene unit for high-performance solution-processed organic solar cells. *Journal of the American Chemical Society* **2012,** *134* (39), 16345-16351.

12.   Ge, J.; Hong, L.; Song, W.; Xie, L.; Zhang, J.; Chen, Z.; Yu, K.; Peng, R.; Zhang, X.; Ge, Z., Solvent annealing enables 15.39% efficiency all-small-molecule solar cells through improved molecule interconnection and reduced non-radiative loss. *Advanced Energy Materials* **2021,** *11* (22), 2100800.

13.   Shan, T.; Ding, K.; Yu, L.; Wang, X.; Zhang, Y.; Zheng, X.; Chen, C. C.; Peng, Q.; Zhong, H., Spatially orthogonal 2D sidechains optimize morphology in all-small-molecule organic solar cells. *Advanced Functional Materials* **2021,** *31* (24), 2100750.

14.   Xiao, L.; Yan, C.; Li, Z.; Zhong, W.; Tan, W.; Liu, Y.; Liu, F.; Peng, X.; Min, Y., Morphology evolution induced by sequential annealing enabling enhanced efficiency in all-small molecule solar cells. *ACS Applied Energy Materials* **2021,** *4* (4), 4234-4241.

15.   Sun, R.; Wu, Y.; Guo, J.; Luo, Z.; Yang, C.; Min, J., High-efficiency all-small-molecule organic solar cells based on an organic molecule donor with an asymmetric thieno [2, 3-f] benzofuran unit. *Science China Chemistry* **2020,** *63*, 1246-1255.

16.   Hu, D.; Tang, H.; Karuthedath, S.; Chen, Q.; Chen, S.; Khan, J. I.; Liu, H.; Yang, Q.; Gorenflot, J.; Petoukhoff, C. E., A volatile solid additive enables oligothiophene all-small-molecule organic solar cells with excellent commercial viability. *Advanced Functional Materials* **2023,** *33* (6), 2211873.

17.   Yi, J.; Zhang, G.; Yu, H.; Yan, H., Advantages, challenges and molecular design of different material types used in organic solar cells. *Nature Reviews Materials* **2024,** *9* (1), 46-62.

18.   Scharber, M. C.; Mühlbacher, D.; Koppe, M.; Denk, P.; Waldauf, C.; Heeger, A. J.; Brabec, C. J., Design rules for donors in bulk-heterojunction solar cells—Towards 10% energy-conversion efficiency. *Advanced materials* **2006,** *18* (6), 789-794.

19.   Elumalai, N. K.; Uddin, A., Open circuit voltage of organic solar cells: an in-depth review. *Energy & Environmental Science* **2016,** *9* (2), 391-410.

20.   Poelking, C.; Tietze, M.; Elschner, C.; Olthof, S.; Hertel, D.; Baumeier, B.; Würthner, F.; Meerholz, K.; Leo, K.; Andrienko, D., Impact of mesoscale order on open-circuit voltage in organic solar cells. *Nature materials* **2015,** *14* (4), 434-439.

21.   Le Bahers, T.; Adamo, C.; Ciofini, I., A qualitative index of spatial extent in charge-transfer excitations. *Journal of chemical theory and computation* **2011,** *7* (8), 2498-2506.

22.   Kohn, W.; Sham, L. J., Self-consistent equations including exchange and correlation effects. *Physical review* **1965,** *140* (4A), A1133.

23.   Frisch, M. J.; Trucks, G. W.; Schlegel, H. B.; Scuseria, G. E.; Robb, M. A.; Cheeseman, J. R.; Scalmani, G.; Barone, V.; Mennucci, B.; Petersson, G. A., Gaussian 09, Revision D. 01, Gaussian, Inc., Wallingford CT. *See also: URL: http://www.gaussian.com* **2009,** *620*.

24.   Casida, M. E., Time-dependent density functional response theory for molecules. In *Recent Advances In Density Functional Methods: (Part I)*, World Scientific: 1995; pp 155-192.

25.   Becke, A. D., Density-functional thermochemistry. I. The effect of the exchange-only gradient correction. *The Journal of chemical physics* **1992,** *96* (3), 2155-2160.

26.   Ochterski, J. W.; Petersson, G. A.; Montgomery Jr, J. A., A complete basis set model chemistry. V. Extensions to six or more heavy atoms. *The Journal of chemical physics* **1996,** *104* (7), 2598-2619.

27.   Tenderholt, A., PyMOlyze, Version 1.1, in Stanford University. *Stanford* **2006,** *4*, 580-592.

796   28.   Tomasi, J.; Mennucci, B.; Cancès, E., The IEF version of the PCM solvation method:
797   an overview of a new method addressed to study molecular solutes at the QM ab initio level.
798   *Journal of Molecular Structure: THEOCHEM* **1999,** *464* (1-3), 211-226.
799   29.   Liu, X.; Ma, S.; Ding, Y.; Gao, J.; Liu, X.; Yao, J.; Dai, S., Molecular engineering of
800   simple carbazole-triphenylamine hole transporting materials by replacing benzene with
801   pyridine unit for perovskite solar cells. *Solar Rrl* **2019,** *3* (5), 1800337.
802   30.   Mester, D.; Kállay, M., Charge-transfer excitations within density functional theory:
803   How accurate are the most recommended approaches? *Journal of Chemical Theory and*
804   *Computation* **2022,** *18* (3), 1646-1662.
805   31.   Guido, C. A.; Cortona, P.; Mennucci, B.; Adamo, C., On the metric of charge transfer
806   molecular excitations: a simple chemical descriptor. *Journal of chemical theory and*
807   *computation* **2013,** *9* (7), 3118-3126.
808   32.   Coppola, F.; Cimino, P.; Raucci, U.; Chiariello, M. G.; Petrone, A.; Rega, N., Exploring
809   the Franck–Condon region of a photoexcited charge transfer complex in solution to interpret
810   femtosecond stimulated Raman spectroscopy: Excited state electronic structure methods to
811   unveil non-radiative pathways. *Chemical science* **2021,** *12* (23), 8058-8072.
812   33.   Coppola, F.; Cimino, P.; Petrone, A.; Rega, N., Evidence of excited-state vibrational
813   mode governing the photorelaxation of a charge-transfer complex. *The Journal of Physical*
814   *Chemistry A* **2024,** *128* (9), 1620-1633.
815   34.   Sini, G.; Sears, J. S.; Brédas, J.-L., Evaluating the performance of DFT functionals in
816   assessing the interaction energy and ground-state charge transfer of donor/acceptor complexes:
817   tetrathiafulvalene− tetracyanoquinodimethane (TTF− TCNQ) as a model case. *Journal of*
818   *Chemical Theory and Computation* **2011,** *7* (3), 602-609.
819   35.   Lu, T.; Chen, F., Multiwfn: A multifunctional wavefunction analyzer. *Journal of*
820   *computational chemistry* **2012,** *33* (5), 580-592.
821   36.   Hutchison, G. R.; Ratner, M. A.; Marks, T. J., Hopping transport in conductive
822   heterocyclic oligomers: reorganization energies and substituent effects. *Journal of the*
823   *American Chemical Society* **2005,** *127* (7), 2339-2350.
824   37.   Marcus, R. A., Chemical and electrochemical electron-transfer theory. *Annual review*
825   *of physical chemistry* **1964,** *15* (1), 155-196.
826   38.   Payne, A.-J.; McCahill, J. S.; Welch, G. C., Indoloquinoxaline as a terminal building
827   block for the construction of π-conjugated small molecules relevant to organic electronics.
828   *Dyes and Pigments* **2015,** *123*, 139-146.
829   39.   Brédas, J.-L.; Norton, J. E.; Cornil, J.; Coropceanu, V., Molecular understanding of
830   organic solar cells: the challenges. *Accounts of chemical research* **2009,** *42* (11), 1691-1699.
831   40.   Coughlin, J. E.; Henson, Z. B.; Welch, G. C.; Bazan, G. C., Design and synthesis of
832   molecular donors for solution-processed high-efficiency organic solar cells. *Accounts of*
833   *chemical research* **2014,** *47* (1), 257-270.
834   41.   Zou, X.; Wen, G.; Hu, R.; Dong, G.; Zhang, C.; Zhang, W.; Huang, H.; Dang, W., An
835   insight into the excitation states of small molecular semiconductor Y6. *Molecules* **2020,** *25*
836   (18), 4118.
837   42.   Yan, C.; Barlow, S.; Wang, Z.; Yan, H.; Jen, A. K.-Y.; Marder, S. R.; Zhan, X., Non-
838   fullerene acceptors for organic solar cells. *Nature Reviews Materials* **2018,** *3* (3), 1-19.
839   43.   Akram, W.; Walayat, A.; Zahid, W. A.; Khan, G. S.; Alanazi, M. M.; Elmushyakhi, A.;
840   Iqbal, J., Rational design and engineering of terminal functional groups in
841   dibenzothiophene-diphenylamine small molecular electron donors for enhanced photovoltaic
842   efficiency in all-small-molecule organic solar cells. *Advanced Theory and Simulations* **2024,** *7*
843   (8), 2400289.
844   44.   Zaier, R.; Martel, A.; Antosiewicz, T. J., Effect of benzothiadiazole-based π-spacers on
845   fine-tuning of optoelectronic properties of oligothiophene-core donor materials for efficient

organic solar cells: a DFT study. *The Journal of Physical Chemistry A* **2023,** *127* (50), 10555-10569.

45. Murugan, P.; Hu, T.; Hu, X.; Chen, Y., Advancements in organic small molecule hole-transporting materials for perovskite solar cells: past and future. *Journal of Materials Chemistry A* **2022,** *10* (10), 5044-5081.

46. Ceriani, C.; Corsini, F.; Mattioli, G.; Mattiello, S.; Testa, D.; Po, R.; Botta, C.; Griffini, G.; Beverina, L., Sustainable by design, large Stokes shift benzothiadiazole derivatives for efficient luminescent solar concentrators. *Journal of Materials Chemistry C* **2021,** *9* (41), 14815-14826.

47. Khasbaatar, A.; Xu, Z.; Lee, J.-H.; Campillo-Alvarado, G.; Hwang, C.; Onusaitis, B. N.; Diao, Y., From solution to thin film: molecular assembly of π-conjugated systems and impact on (opto) electronic properties. *Chemical reviews* **2023,** *123* (13), 8395-8487.

48. Han, G.; Yi, Y., Origin of photocurrent and voltage losses in organic solar cells. *Advanced Theory and Simulations* **2019,** *2* (8), 1900067.

49. Menke, S. M.; Ran, N. A.; Bazan, G. C.; Friend, R. H., Understanding energy loss in organic solar cells: toward a new efficiency regime. *Joule* **2018,** *2* (1), 25-35.

50. Pei, K.; Wu, Y.; Islam, A.; Zhang, Q.; Han, L.; Tian, H.; Zhu, W., Constructing high-efficiency D−A−π−A-featured solar cell sensitizers: a promising building block of 2,3-diphenylquinoxaline for antiaggregation and photostability. *ACS Applied Materials & Interfaces* **2013,** *5* (11), 4986-4995.

51. Li, S.; Li, W.; Ma, J., Generalized energy-based fragmentation approach and its applications to macromolecules and molecular aggregates. *Accounts of chemical research* **2014,** *47* (9), 2712-2720.

52. Wei, N.; Guo, Y.; Song, H.; Liu, Y.; Lu, H.; Bo, Z., Reducing non-radiative energy losses in non-fullerene organic solar cells. *ChemSusChem* **2025,** *18* (6), e202402169.

53. Madhu, M.; Ramakrishnan, R.; Vijay, V.; Hariharan, M., Free charge carriers in homo-sorted π-stacks of donor–acceptor conjugates. *Chemical Reviews* **2021,** *121* (13), 8234-8284.

54. Zhang, K. N.; Du, X. Y.; Yan, L.; Pu, Y. J.; Tajima, K.; Wang, X.; Hao, X. T., Organic photovoltaic stability: understanding the role of engineering exciton and charge carrier dynamics from recent progress. *Small Methods* **2024,** *8* (2), 2300397.

55. Naveed, H. B.; Zhou, K.; Ma, W., Interfacial and bulk nanostructures control loss of charges in organic solar cells. *Accounts of Chemical Research* **2019,** *52* (10), 2904-2915.

56. Han, G.; Yi, Y.; Shuai, Z., From molecular packing structures to electronic processes: theoretical simulations for organic solar cells. *Advanced Energy Materials* **2018,** *8* (28), 1702743.

57. Kong, X.; He, T.; Qiu, H.; Zhan, L.; Yin, S., Progress in organic photovoltaics based on green solvents: from solubility enhancement to morphology optimization. *Chemical Communications* **2023,** *59* (81), 12051-12064.

58. Han, J.; Xu, H.; Paleti, S. H. K.; Sharma, A.; Baran, D., Understanding photochemical degradation mechanisms in photoactive layer materials for organic solar cells. *Chemical Society Reviews* **2024,** *53* (14), 7426-7454.

59. Lan, J.-L.; Liu, X.-N.; Xiao, C.-N.; Sui, M.-Y.; Sun, G.-Y., Correction of the calculation method of CT state energy in ITIC and Y6 acceptor systems. *Journal of Photochemistry and Photobiology A: Chemistry* **2024,** *456*, 115821.

60. Yang, J.; Wu, X.; Li, Q.-S.; Li, Z.-S., Boron-based non-fullerene small molecule acceptors via nitrogen substitution: a theoretical study. *Materials Advances* **2022,** *3* (7), 3229-3237.

The data supporting this article have been included as part of the Supplementary Information.